Robust poor man's Majorana zero modes using Yu-Shiba-Rusinov states

Zatelli, Francesco; van Driel, David; Xu, Di; Wang, Guanzhong; Liu, Chun-Xiao; Bordin, Alberto; Roovers, Bart; Mazur, Grzegorz P.; van Loo, Nick; Wolff, Jan C.

DOI
10.1038/s41467-024-52066-2

Publication date
2024

Document Version
Final published version

Published in
Nature Communications

nature communications

Article

https://doi.org/10.1038/s41467-024-52066-2

Robust poor man's Majorana zero modes using Yu-Shiba-Rusinov states

Received: 2 July 2024

Accepted: 21 August 2024

Published online: 11 September 2024

Check for updates

Francesco Zatelli[1,3], David van Driel[1,3], Di Xu[1,3], Guanzhong Wang[1,3], Chun-Xiao Liu[1], Alberto Bordin[1], Bart Roovers[1], Grzegorz P. Mazur[1], Nick van Loo[1], Jan C. Wolff[1], A. Mert Bozkurt[1], Ghada Badawy[2], Sasa Gazibegovic[2], Erik P. A. M. Bakkers[2], Michael Wimmer[1], Leo P. Kouwenhoven[1] ✉ & Tom Dvir[1]

Kitaev chains in quantum dot-superconductor arrays are a promising platform for the realization of topological superconductivity. As recently demonstrated, even a two-site chain can host Majorana zero modes known as "poor man's Majorana". Harnessing the potential of these states for quantum information processing, however, requires increasing their robustness to external perturbations. Here, we form a two-site Kitaev chain using Yu-Shiba-Rusinov states in proximitized quantum dots. By deterministically tuning the hybridization between the quantum dots and the superconductor, we observe poor man's Majorana states with a gap larger than 70 μeV. The sensitivity to charge fluctuations is also greatly reduced compared to Kitaev chains made with non-proximitized dots. The systematic control and improved energy scales of poor man's Majorana states realized with Yu-Shiba-Rusinov states will benefit the realization of longer Kitaev chains, parity qubits, and the demonstration of non-Abelian physics.

Kitaev chains based on quantum dots (QDs) coupled via a hybrid semiconductor-superconductor heterostructure are a promising avenue for the creation of Majorana bound states[1,2]. Even a minimal chain, consisting of only two QDs, supports fine-tuned Majorana zero modes known as "poor man's Majoranas" (PMMs)[3]. These PMM states do not benefit from topological protection, but already exhibit robustness to local perturbations and quadratic protection from global fluctuations in the chemical potential[3]. Moreover, PMM states obey non-Abelian exchange statistics, thus providing a favorable platform for braiding and Majorana-based qubit experiments in the near future[4–7].

One approach to form PMM states is to couple spin-polarized QDs via both crossed Andreev reflection (CAR) and elastic cotunneling (ECT)[2,3,8,9], as recently demonstrated in InSb/Al nanowires[10]. Realizing such a system is challenging since the coupling between the QDs and the superconducting reservoir that enables ECT and CAR needs to be balanced. Too small a coupling results in negligible interaction between the QDs, while too large a coupling prevents their charge from being a good quantum number. While ref. 10 provided the necessary proof of concept, the gap separating PMMs from excited states was not much higher than the electron temperature. Furthermore, appreciable noise in the measured spectra indicated sensitivity to charge fluctuations, setting dim prospects for a qubit realization. Finally, a strong coherent coupling between the QDs was observed only in a limited number of devices, posing a significant yield challenge in realizing longer Kitaev chains and coupling them.

In this work, we show that it is possible to overcome these challenges by using spin-polarized Yu-Shiba-Rusinov (YSR) states[11–20] instead of non-proximitized QDs as the sites of a Kitaev chain[21–30]. We systematically control the hybridization between two QDs and a superconductor to form strongly coupled YSR states, which we use to realize a robust two-site Kitaev chain[21,31]. We demonstrate that we can

[1]QuTech and Kavli Institute of NanoScience, Delft University of Technology, Delft, The Netherlands. [2]Department of Applied Physics, Eindhoven University of Technology, Eindhoven, The Netherlands. [3]These authors contributed equally: Francesco Zatelli, David van Driel, Di Xu, Guanzhong Wang.
✉e-mail: l.p.kouwenhoven@tudelft.nl

tune the system to a sweet spot hosting PMMs without relying on microscopic, device-specific details. Importantly, the PMMs do not hybridize despite their significant wavefunction overlap in the superconductor originating from its strong coupling to the QDs[21,31]. We show that the sensitivity of the resulting PMMs to charge fluctuations affecting the QDs decreases by two orders of magnitude compared to a QD-based Kitaev chain[10]. In addition, we measure a gap between ground and excited states of E_{gap} = 76 μeV, a threefold increase compared to our previous report[10].

We present results obtained using a hybrid semiconducting InSb nanowire partly covered with a superconducting Al film. However, our approach does not rely on the details of the material platform. Complementary results are also reported in a parallel study on a 2D hybrid platform using an InAsSb/Al two-dimensional electron gas[32], demonstrating the wider applicability of our approach.

Results

Fabrication and setup

Figure 1a shows a scanning electron microscope image of the reported device. It consists of an InSb nanowire (green) placed on top of a series of bottom gates[33]. The middle part of the nanowire is covered by a thin Al shell (blue), forming a superconductor-semiconductor hybrid whose electrochemical potential is controlled by a plunger gate (V_H). On both sides of the hybrid segment, QDs are formed in the nanowire using three gates each. The electrochemical potential of each QD is controlled by a plunger gate (V_{LP} and V_{RP} for the left and right QDs,

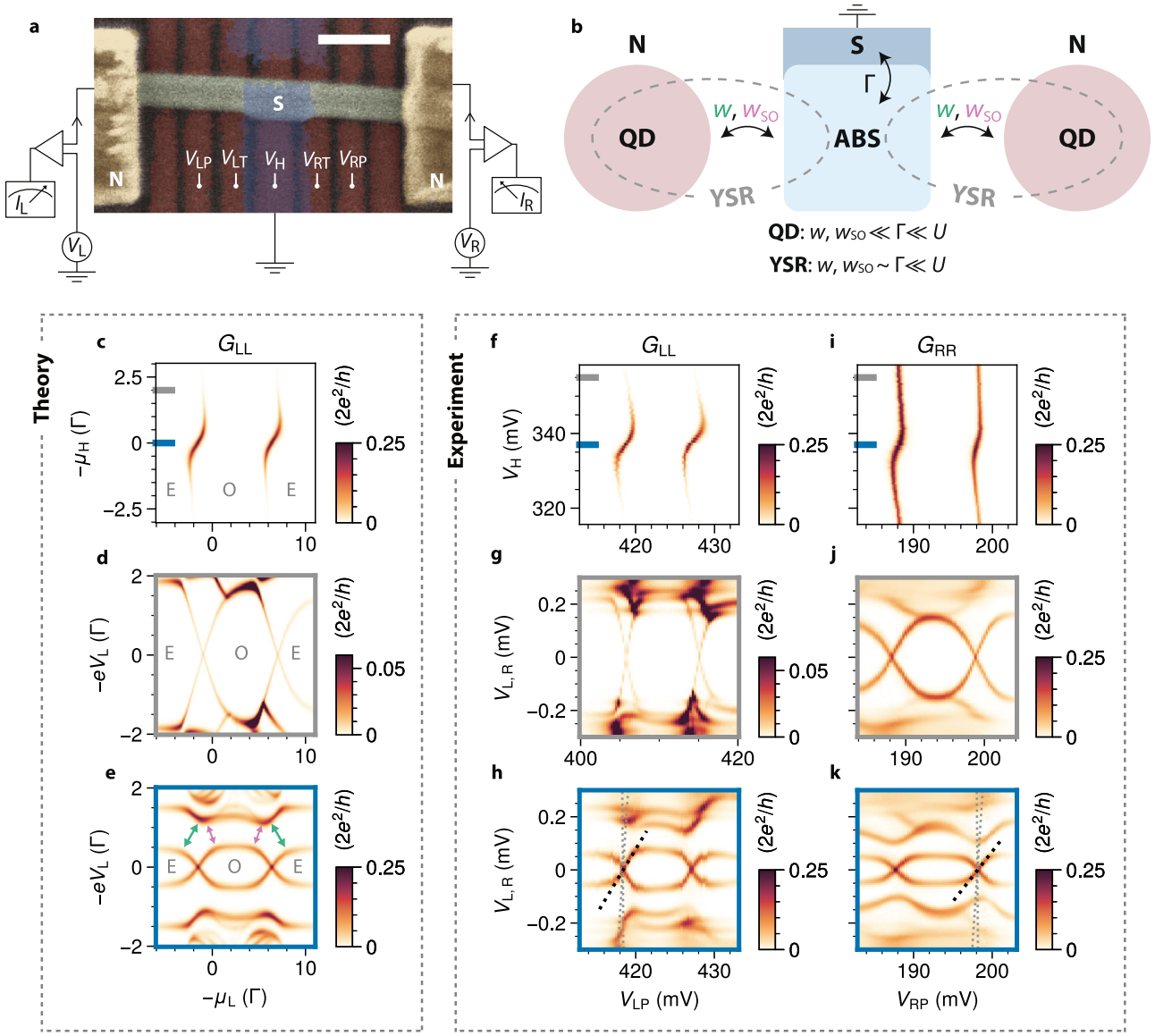

Fig. 1 | YSR states formed by hybridizing QDs with an ABS. a False-colored scanning electron micrograph and measurement circuit of the device. Scale bar is 200 nm. **b** Illustration of the QD-ABS-QD model. Two QDs are coupled to the same ABS via spin-conserving and spin-flipping tunneling. QD and YSR regimes are defined by the relative energy scales shown below the sketch. **c** Numerical CSD using zero-bias conductance of a QD coupled to an ABS. "E"/"O" indicate even/odd occupation of the QD. **d**, **e** Numerical conductance spectrum of a QD coupled to an ABS as a function of QD chemical potential when ABS is far (**d**) and close to its energy minimum (**e**). In **e**, green/pink arrows indicate avoided crossings due to spin-conserving/spin-flipping tunneling. **f**, **h** Same as **c**–**e** for the left QD coupled to an ABS, experimentally measured using local conductance. Gray/blue ticks in **f** mark V_H values at which **g**/**h** are measured. The right QD is off resonance. In **h**, we extract a lever arm $\alpha \approx 0.05e$ by fitting the spectrum with the black dotted line at the zero-energy crossing. This procedure overestimates the actual lever arm since it does not account for capacitance to the normal lead. For comparison, we plot the profile of a typical Coulomb diamond in our device with gray dotted lines (Supplementary Fig. 3a). The V_{LP} range in **g** is shifted because of a gate jump affecting the left QD. **i**–**k**, Same as **f**–**h**, but for the right QD. The extracted lever arm is $\alpha \approx 0.04e$.

respectively), and the couplings between the QDs and the hybrid are controlled by tunnel gates (V_{LT} and V_{RT} for the left and right QDs, respectively). A normal lead is attached to each QD, separated by another gate-defined tunnel barrier. The superconducting lead is kept grounded at all times. In addition, the two normal leads are connected to off-chip multiplexed resonators for fast RF reflectometry measurements[34], using the setup described in ref. 35. Each lead is voltage-biased independently with respect to the grounded Al, with voltages V_L and V_R on the left and right leads, respectively. The currents (I_L and I_R on the left and right leads), the local conductances ($G_{LL} = dI_L/dV_L$, $G_{RR} = dI_R/dV_R$), and the non-local conductances ($G_{RL} = dI_R/dV_L$, $G_{LR} = dI_L/dV_R$) are measured simultaneously. When the full conductance matrix is measured, we correct for line resistance as described in the Methods section. Further fabrication and setup details can be found in our previous publications[36–38]. The experiment is conducted in a dilution refrigerator with a base temperature of 30 mK. A magnetic field of $B = 150$ mT is applied along the nanowire axis, inducing a Zeeman splitting of ~200 μeV in the QDs (Supplementary Fig. 1).

YSR states in quantum dots

We model our system using a three-site model in which the hybrid is considered as a single Andreev bound state (ABS) in the atomic limit[15,16] tunnel-coupled to two QDs (see schematics in Fig. 1b)[21]. The QDs have charging energy U, Zeeman splitting E_Z, and chemical potentials μ_L, μ_R for the left and right QD, respectively. The ABS has an induced gap Γ, which in the atomic limit[15,16] can be identified with its tunnel coupling to the bulk superconductor. Its charging energy is negligible compared to the induced gap Γ due to the screening of the grounded Al film. It also has Zeeman splitting E_{ZH}, which is smaller than that of the QDs due to metallization of the ABS[39]. We ensure $E_{ZH} < \Gamma$ so that the ground state of the ABS is always a BCS singlet. The electron-hole composition of the ABS depends on its chemical potential μ_H.

In our model, the QDs are coupled to the ABS by spin-conserving and spin-flipping tunneling due to spin-orbit interaction, with amplitudes w and w_{SO}, respectively[21]. The hybridization between QDs and the ABS becomes significant when w, $w_{SO} \sim \Gamma$. As a consequence, the QDs become proximitized and form YSR states[20,31], which we distinguish from ABSs because of their large charging energy[15–19,40]. We refer readers to Supplementary Notes 1 and 2 and the parallel work of ref. 31 for a more detailed discussion of the distinction between ABSs and YSR states, and for theory models to describe the strong coupling regime investigated in this work.

To understand the nature of the YSR states formed in proximitized QDs, we first examine the coupling between a single QD and an ABS in the hybrid segment, following ref. 20. Fig. 1c shows the theoretical zero-bias conductance of a QD-ABS charge stability diagram (CSD), while the second QD is off-resonance. The two vertical features indicate parity transitions of the system, largely corresponding to the consecutive filling of a single orbital of the QD by two electrons. The S-shaped conductance features result from renormalization of the QD energy via hybridization with the ABS. The ABS reaches its energy minimum at charge neutrality, i.e., $\mu_H = 0$, where its excitation is equal-parts electron and hole. The hybridization with the QD is also maximal here due to their minimal energy separation, evident in the enhanced zero-bias conductance as local Andreev reflection becomes stronger[20,31]. The QD spectra in panels d and e further reveal its hybridization with the ABS. When the latter is away from charge neutrality, the QD spectrum as a function of μ_L (Fig. 1d) exhibits straight features reminiscent of Coulomb diamonds. As the ABS approaches $\mu_H = 0$ (Fig. 1e), such features evolve into an eye-shaped spectrum typical of YSR states[19,41–44]. The arrows indicate avoided crossings in the excited states of the spectrum produced by spin-conserving (green) and spin-flipping (pink) tunneling between the ABS and the QD levels[31].

The hybrid segment of our device features multiple discrete ABSs well-separated from each other in V_H (Supplementary Fig. 2). We operate in a V_H range containing a single ABS level. In Fig. 1f, we show the zero-bias conductance measured with the left lead as a function of V_{LP} and V_H. V_{RP} is fixed to keep the right QD off-resonance. We observe the QD-ABS charge stability diagram features described in panel c, indicating the presence of an ABS reaching its energy minimum at $V_H \approx 337$ mV. The QD-ABS hybridization is further confirmed by the QD spectrum being in agreement with the model when the ABS is away from (Fig. 1g) and at its energy minimum (Fig. 1h).

The YSR zero-energy excitations in Fig. 1h are our building blocks of a Kitaev chain. Compared to a non-proximitized QD zero-energy crossing, these YSR crossings have noticeably weaker energy dispersion as a function of gate (see dashed lines in panel h). To quantify this observation, we can estimate the lever arm of the YSR excitation at charge degeneracy using its gate-dispersion slope: $\alpha \equiv \partial E/\partial V_{LP}$. In contrast to the above-gap QD lever arm of $\alpha \approx 0.4e$ in our devices (Supplementary Fig. 3a), this subgap lever arm reduces to $\alpha \approx 0.2e$ (Supplementary Fig. 3b) when the ABS is detuned from its charge neutrality. Tuning the ABS to its energy minimum further reduces the lever arm to $\alpha \approx 0.05e$ (Fig. 1h). This signals a strong reduction in the effective charge of the fermionic excitation, attributable to charging energy renormalization, QD-ABS hybridization, and electron-hole superposition[45,46], as detailed in Supplementary Fig. 4.

The right QD shows similar behavior when coupled to the same ABS (Fig. 1i–k). However, when the ABS is away from charge neutrality, the subgap conductance is not significantly suppressed (Fig. 1i) and the QD spectrum still shows typical YSR features (Fig. 1h), albeit with a small superconducting coupling. This could be due to residual proximity resulting from direct coupling between the QD and the superconducting film since V_H does not affect it appreciably (Supplementary Fig. 5).

Coupled YSR states

Recent theoretical[8,21] and experimental[9,10,47] works have shown that an ABS can mediate elastic co-tunneling (ECT) and crossed Andreev reflection (CAR) between QDs. These two processes implement the hopping and pairing terms of the original Kitaev chain model[1,2]. To form PMM states in a two-site chain, the amplitudes of both terms must be equal[3]. Such control can be achieved by tuning the electrochemical potential of the ABS in the hybrid nanowire[8–10,21].

Similar effective ECT and CAR couplings, with respective amplitudes t and Δ, also emerge between YSR states (Fig. 2a) formed by strongly coupling QDs to the same ABS[31,48,49]. To observe them, we turn to the CSD of two such YSR states, akin to those explored in refs. 50,51. In Fig. 2b, we show the zero-bias conductance matrix measured as a function of V_{RP} and V_{LP} when the ABS is tuned away from its energy minimum. All elements of the conductance matrix show prominent resonances arising from the two charge transitions of each QD. The type of avoided crossings observed in the CSD serves as an indication of the coupled-YSR system's ground state[10,21]. Avoided crossings along a negative diagonal, as seen in all four resonances in Fig. 2b, show hybridization between states with the same total charge. This is the ground state of the system when $t > \Delta$. This observation is further confirmed by the negative non-local conductance that is characteristic of ECT[10].

Increasing the value of V_H leads to a change in the CSD, shown in Fig. 2c. Here, the bottom-left and the top-right resonances show avoided crossings along a positive diagonal associated with $\Delta > t$. In the top-left and bottom-right, the resonance lines cross each other, indicating a PMM sweet spot, with $t \approx \Delta$. Finally, bringing the ABS close to its energy minimum by a further increase of V_H tunes all of the quadrants of the CSD to the $\Delta > t$ regime (Fig. 2d). The theoretical model reproduces the observed evolution of the CSDs (Supplementary Fig. 6a–c).

https://doi.org/10.1038/s41467-024-52066-2

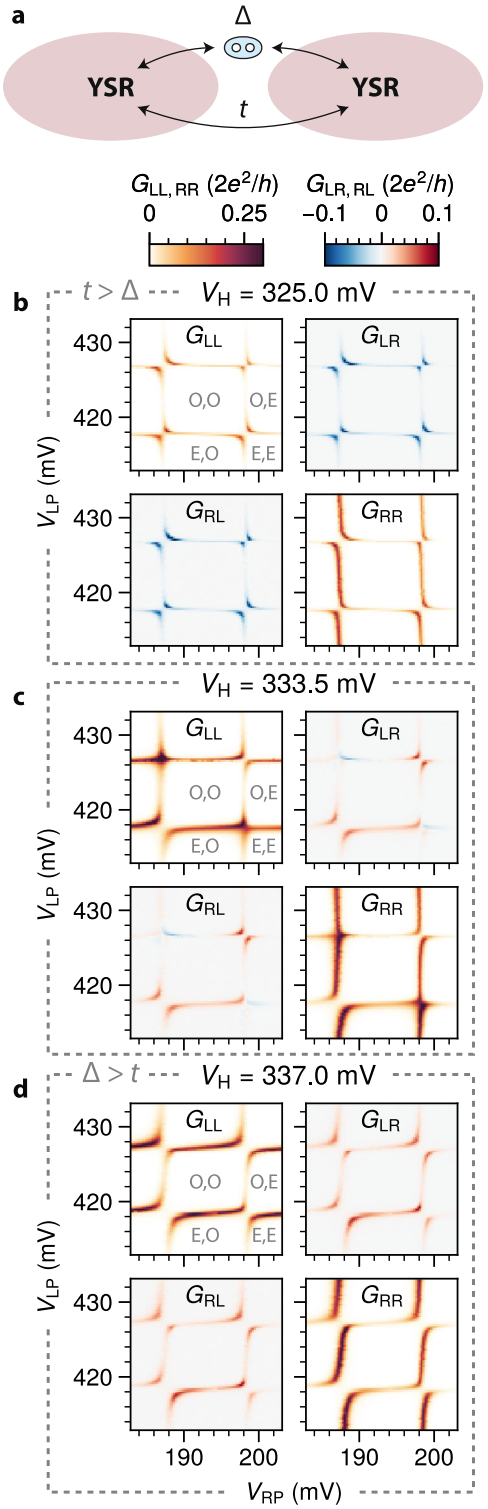

Fig. 2 | ECT and CAR coupling between YSR states. a Illustration of the effective two-site system of YSR states coupled via ECT (t) and CAR (Δ). **b**–**d** Conductance matrices of CSDs measured at different V_H. By tuning the electrochemical potential of the ABS in the hybrid, it is possible to continuously vary t and Δ. In **b**, avoided crossings along the antidiagonal are observed, indicating $t > \Delta$. The opposite regime is shown in **d**, with all the avoided crossings along the diagonal, indicating $t < \Delta$. The crossover between these two regimes is shown in **c**, where two crossings indicate $t \approx \Delta$.

Gate control of CAR and ECT

ABS-mediated ECT and CAR couplings between QDs are controlled by the chemical potential of ABS[8,9]. At the energy minimum of the ABS, its excitation is equally electron- and hole-like, both parts interfering constructively to enhance CAR and destructively to quench ECT. Finite values of μ_H lead to an imbalance between the electron and hole parts of the ABS, decreasing the value of the CAR coupling while enhancing ECT. This control over the ECT and CAR amplitudes guarantees a PMM sweet spot when the two QDs are coupled via a single ABS[8,9,21]. To demonstrate that this description can be extended to YSR states coupled via an ABS, we study how the couplings t and Δ vary as the electrochemical potential of the ABS changes.

The magnitudes of t and Δ can be extracted by measuring the excitation spectrum of the system at $\mu_L = \mu_R = 0$, when spectral splitting is determined by the couplings alone. We limit the discussion here to the bottom-right crossing of Fig. 2, where the QDs' spins are opposite. Other crossings exhibit qualitatively similar behavior (Supplementary Fig. 7). At each fixed value of V_H, we measure a CSD (Fig. 3a) and set the QD gates to the center of an avoided crossing. There, the subgap spectrum exhibits two sets of electron-hole symmetric peaks at energies $|t - \Delta|$ and $t + \Delta$ (Fig. 3b), as detailed in Methods. By fitting the measured spectrum with two pairs of Gaussians symmetric around $V_{L,R} = 0$, we extract the energy of the excited states and calculate t and Δ. We repeat this procedure for different values of V_H and collect the spectra in Fig. 3c, where each line was measured as described above.

Figure 3 d shows the extracted values of ECT and CAR amplitudes. At $V_H \approx 322$ mV and $V_H \approx 355$ mV, the outer peaks almost merge with the inner ones, indicating $|t - \Delta| \approx t + \Delta$. Inspecting the corresponding CSDs (see Fig. 2b for an example, all the CSDs are available in the online repository), we can see that ECT is dominant and, therefore, $t \gg \Delta$. Upon varying V_H, the two peaks split into four well-separated peaks, signaling that CAR is increasing although ECT still prevails. At $V_H \approx 333$ mV and 345 mV, the two inner peaks merge into a single zero-bias peak. These are two sweet spots where $t \approx \Delta$. In between them, CAR dominates, as the CSDs can confirm (Fig. 2d). Around $V_H \approx 338$ mV, the outer peaks merge again, this time indicating $\Delta \gg t$. This feature is the peak in Δ and dip in t seen in Fig. 3d, because of the aforementioned interference effects[8,9]. Finally, Supplementary Fig. 6d shows that the same spectral features are reproduced by the theoretical model.

The zero-energy crossings in Fig. 3e allow us to characterize the robustness of the PMM sweet spots to charge fluctuations affecting the ABS and, consequently, t and Δ, causing a splitting of the zero-energy states. Indeed, we observe that each zero-energy state splits with a linear dependence on V_H as predicted by theory, indicating the lack of protection against deviations from the condition $t = \Delta$ known for a two-site Kitaev chain[3]. We extract a slope of $\frac{\partial E}{\partial V_H} \approx 7\,\mu$eV/mV and 3 μeV/mV for the two crossings, comparable to what we measured in ref. 10.

Majorana sweet spot

Finally, we measure the spectrum and stability of the PMM states against perturbation of the QDs. We tune our device to the sweet spot at $V_H = 333.5$ mV, where $t \approx \Delta$. In Fig. 4a, we show the full conductance matrix of the CSD at the sweet spot. As expected, the resonance lines cross each other and non-local conductance alternates between positive and negative values. The spectrum measured at the sweet spot in the center of the CSD (Fig. 4b) shows, on both sides of the device, a zero-bias conductance peak clearly separated from the excited states. As a result of the much stronger coupling between YSR states, the first excited states reside at energies of $E_{gap} \approx 76$ μeV, three times larger than in our previous report[10] and significantly above the electron temperature.

One of the hallmarks of PMM states is their stability against local perturbations of the QDs' electrochemical potential. In Fig. 4c, we measure the spectrum of the QDs varying V_{RP} while keeping the left QD on resonance. The observed zero-bias conductance peak persists until

https://doi.org/10.1038/s41467-024-52066-2

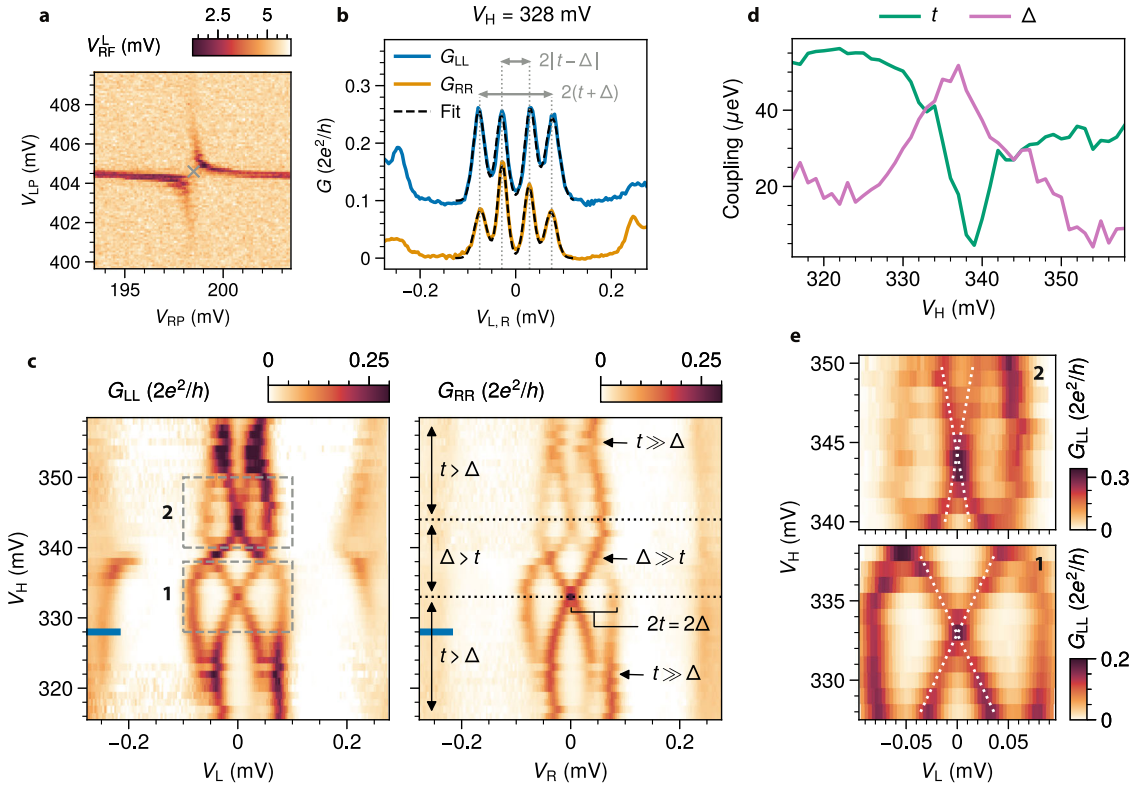

Fig. 3 | ECT and CAR coupling as a function of the ABS chemical potential. a CSD measured using RF reflectometry. The center of the avoided crossing, marked with a gray cross, is identified as $\mu_L = \mu_R = 0$. **b** Spectrum measured on both sides of the device at the center of the avoided crossing shown in **a**. The inner peaks correspond to excited states at $|t - \Delta|$, while the outer ones correspond to excited states at $t + \Delta$. By summing and subtracting these energies, it is possible to extract t and Δ for each V_H value. **c** Spectrum as a function of V_H while $\mu_L = \mu_R = 0$. Each line of the spectrum was measured as described above. The blue tick indicates the V_H value at which **a** and **b** were measured. **d** ECT and CAR couplings extracted from **c**. **e** Zoom-in on the zero-energy crossings highlighted in **c**. The white dotted lines are fits to extract the slope of the linear splitting. The data reported here was collected for the bottom-right charge transition shown in Fig. 2. More details about data processing and data for all charge degeneracies are reported in Supplementary Fig. 7.

the next charge degeneracies of the detuned QD. The range of this region is determined by its charging energy and level spacing. For our device, this corresponds to a gate range of ~10 mV (Fig. 2c). Tuning V_{LP} while keeping the right QD on resonance (Supplementary Fig. 8b) shows the same qualitative features. The same behavior can be reproducibly observed with other QD and ABS orbitals, as shown in Supplementary Fig. 9.

If the electrochemical potentials of both QDs are detuned from the sweet spot, PMM states are expected to split quadratically. This is verified in Fig. 4d, where we measure the spectrum while detuning both QDs along the antidiagonal path shown in Fig. 4a. The spectrum taken along the diagonal path is shown in Supplementary Fig. 8c. Numerical simulations reproducing these measurements are reported in Supplementary Fig. 6e–i. For comparison, we plot the quadratic dispersion measurements of the QD-based vs YSR-based PMMs side by side in panels e and f. The curvature of the energy-gate dispersion close to the sweet spot is directly proportional to the dephasing rate resulting from charge noise affecting both QDs[52–55] and is therefore a measure of the Majorana states' robustness against it. Comparing the overlaid curves in Fig. 4e, f, we find the gate dispersion curvature reported in this work to be a factor of ~150 lower than the non-proximitized case (details in Methods). This striking reduction can be fully explained by the decreased lever arm of the YSR states, α, and the increased E_{gap}, since the curvature expected from the theory model is α^2/E_{gap} (see "Methods" section).

To illustrate the effect of reduced charge dispersion on the coherence of a potential poor man's Majorana qubit, we calculate the dephasing rates using realistic charge noise estimations and data presented above (see Supplementary Note 3). While perturbation of QDs' potentials is expected to be the dominant mechanism of energy splitting and thus dephasing for non-proximitized PMMs, the drastic reduction in gate dispersion of YSR-based PMMs makes it negligible compared to dephasing caused by deviations from the $t = \Delta$ condition. The estimated $T_2^* \sim 10$ ns is now limited by noise affecting the couplings t and Δ, nearly an order of magnitude higher than the charge-noise-limited T_2^* extracted from data in our previous report[10]. Importantly, the expected dephasing time is now also much longer than the adiabatic limit $\hbar/E_{gap}$ ~ 10 ps, which sets an upper bound on how fast Majorana states can be manipulated without populating the excited states[5,52].

Discussion

In conclusion, we have realized a two-site Kitaev chain hosting PMM states by coupling YSR states via ECT and CAR. We have formed YSR states by coupling QDs to a common ABS. We have shown how controlling their hybridization with the ABS allows us to deterministically achieve the strong coupling regime between the YSR states. By tuning the electrochemical potential of the ABS, we can systematically control the ECT and CAR couplings in accordance with a single-ABS theoretical model. We have demonstrated that, despite the strong hybridization between QDs and ABS, it is possible to tune the system to a regime consistent with PMM states. We emphasize that the strong QD-ABS coupling causes the PMMs' wavefunction to substantially overlap in the hybrid. Nevertheless, such overlap does not cause hybridization between the PMMs themselves[21,31]. The resulting PMM states have two significant improvements over those in a non-proximitized QD chain.

https://doi.org/10.1038/s41467-024-52066-2

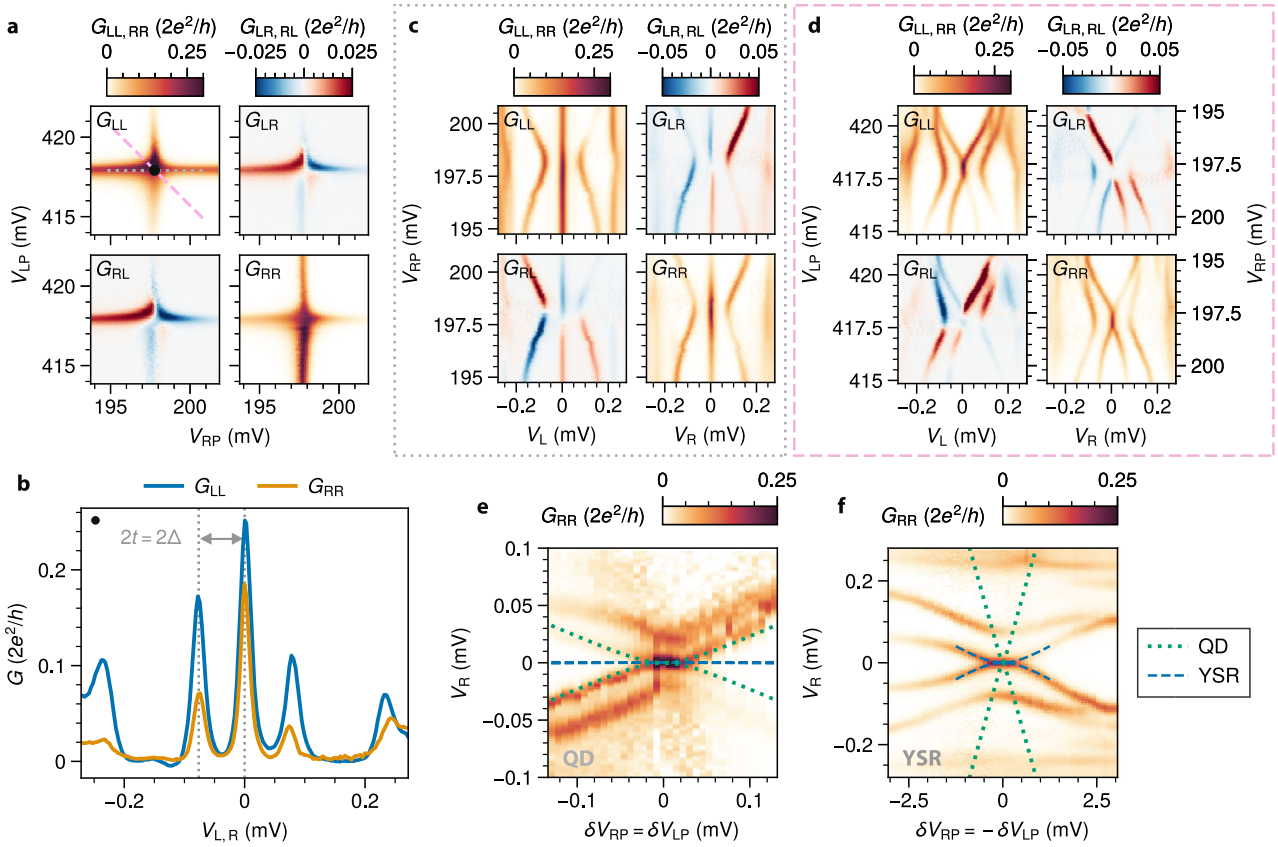

Fig. 4 | Poor man's Majorana sweet spot for coupled YSR states. a Conductance matrix of a crossing in the CSD, when $t \approx \Delta$. **b** Spectrum of both sides measured at the sweet spot in the center of the crossing of panel **a**. **c** Conductance matrix of the spectrum as a function of V_{RP} (along the gray dotted line in **a**). The right QD is detuned across the sweet spot, while the left one is kept on resonance. **d** Conductance matrix of the spectrum measured detuning both QDs simultaneously along the antidiagonal along the pink dashed line in **a**. **e**, **f** G_{RR} as a function of the simultaneous detunings of both sites, δV_{LP} and δV_{RP}, away from the sweet spot, using QDs (**e**, replotted from ref. 10) and YSR states (**f**, from the same dataset presented in **d**). For comparison, we have plotted the two gate dispersions with the same scale in both plots. The green dotted lines correspond to the expected energy splitting of a PMM realized with QDs, the blue dashed lines to that of a PMM realized with YSR states, as detailed in the Methods section.

First, the stronger coupling between the YSR states triples the gap between the PMM and excited states, protecting the former from finite temperature excitations[53] and enabling faster adiabatic operations[5,52]. Second, the reduced charge dispersion of the YSR states enhances the robustness of the PMMs against charge noise affecting both QDs by two orders of magnitude. Thanks to these, even a two-site Kitaev chain realized using YSR states should suffice for a prototypical Majorana qubit and verification of non-Abelian properties with fusion and braiding experiments. Despite the present lack of protection against tunnel-coupling noise, the expected coherence of Majorana qubits made from PMM states is increased by close to an order of magnitude compared to the first report[10]. In the future, increasing the number of sites can mitigate noise affecting the tunnel-coupling rates. Estimations using parameters of the YSR-based PMMs suggest that a Majorana qubit realized with Kitaev chains as short as 3 to 5 sites could already achieve dephasing times comparable to those predicted for continuous nanowires[2,53,56]. Finally, the systematic control of QD-ABS and subsequently YSR-YSR hybridization demonstrated in this work will be useful for Andreev spin qubits[57,58], long-distance coupling of spin qubits via a superconductor[59,60], and analog quantum simulations of Fermi-Hubbard systems[61–63] with superconductivity.

Methods

Device fabrication

The InSb/Al hybrid nanowire device presented in this work was fabricated using the shadow-wall lithography technique[36,37].

A substrate is patterned with Ti/Pd gates. 10 nm of AlO_x and 10nm of HfO_x are deposited by ALD as gate dielectric. HSQ shadow walls are then patterned. Nanowires are deposited and pushed next to the shadow walls using an optical micro-manipulator. An 8nm Al shell is deposited at alternating angles of 15° and 45° with respect to the substrate, followed by a capping layer of 20 nm of AlO_x. Normal leads in ohmic contact with the nanowire are fabricated by Ar milling and evaporation of Cr/Au.

Additional details about the substrate fabrication and the Al deposition are described in ref. 38.

Transport measurements and data processing

The measurements are done in a dilution refrigerator with a base temperature of 30 mK. A magnetic field of 150 mT is applied along the nanowire axis except in Supplementary Fig. 1c, d.

The three-terminal setup used to measure the device is illustrated in Fig. 1a. The SC lead is always kept grounded. The two normal leads can be voltage-biased independently. When a bias is applied to one side, the other one is kept grounded. The currents I_L and I_R are measured separately. Digital multimeters and lock-in amplifiers are used to read the voltage outputs of the current meters. AC excitations of 5 μV RMS are applied on each side with different frequencies (39 Hz on the left and 29 Hz on the right), except for Supplementary Fig. 2 and Supplementary Fig. 5d–f, where excitations of 10 μV RMS were used.

Off-chip multiplexed resonators[34] connected to the two normal leads are used for fast RF reflectometry measurements. This

measurement scheme was employed to speed up the tune-up of the device, for Fig. 3, and for Supplementary Fig. 7, as explained in Fig. 3a. Additional details about the reflectometry setup are described in ref. 35.

Spinless PMM spectrum

The low-energy spectrum of the coupled YSR system arising from the model described in Supplementary Note 1 can be reduced to that of a spinless PMM model[3,6,8,21,31].

In this simplified model, the non negative energy eigenvalues are[3]

$$E_{\pm} = \sqrt{\mu_+^2 + \mu_-^2 + t^2 + \Delta^2 \pm 2\sqrt{(\mu_+^2 + \Delta^2)(\mu_-^2 + t^2)}}, \quad (1)$$

where $\mu_{\pm} = \frac{\mu_L \pm \mu_R}{2}$, μ_L and μ_R are the chemical potentials of the two sites, and t, Δ are the couplings. The spectrum is symmetric around zero energy because of particle-hole symmetry. If $\mu_L = \mu_R = 0$, the eigenvalues reduce to $E_+ = t + \Delta$ and $E_- = |t - \Delta|$. These are the excitation energies that we use to extract t and Δ from the measured spectra in Fig. 3.

The gate dispersion lines plotted in Fig. 4e,f are calculated using the lowest excitation energy. When $t = \Delta$ we obtain

$$E_- = \sqrt{\alpha^2\delta V^2 + 2t^2 - 2\sqrt{t^2(t^2 + \alpha^2\delta V^2)}}, \quad (2)$$

where α is the lever arm converting voltage to chemical potential and δV is the simultaneous detuning of each gate away from the sweet spot. For the PMM realized with QDs, we have used $\alpha = 0.33e$ and $t = 12\,\mu\text{eV}$[10]. For the PMM realized with YSR states we have used $\alpha = 0.05e$ (Supplementary Fig. 1) and $t = 38\,\mu\text{eV}$ (Fig. 4b). Finally, the quadratic splitting of PMM states can be derived by expanding the expression above for small δV, which gives

$$E_- \approx \frac{\alpha^2}{2t}\delta V^2. \quad (3)$$

Series resistance correction

The effect of series resistance in the fridge line and other parts of the circuit on transport measurements of a three-terminal device of our type is described in ref. 64, as well as how to correct it. In our setup, the resistance of the voltage source is 100 Ω and that of the current meter is 200 Ω. Additional series resistance comes from the fridge lines and the ohmic contacts. Correcting for the voltage fall over these resistors in series to the device requires knowledge of the exact resistance values, which we presently cannot obtain before the next sample exchange. Therefore, we make use of the fact that the bulk Al superconducting gap in local conductance measurements should stay constant across all gate values to arrive at an estimation of the total series resistance in each fridge line.

In Supplementary Fig. 10a, c, it is possible to observe that the superconducting gap appears enlarged when there is finite subgap conductance, indicating unaccounted-for series resistance. To estimate it, we correct the G_{LL} measurement shown in Supplementary Fig. 10a for different trial values of the series resistance. We extract the energies of the coherence peaks and calculate their variance. Finally, we choose the value that minimizes the variance as the optimal series resistance. We find an optimal value of 3.65 kΩ, in addition to the resistance of the voltage source and current meter. The corrected measurement is shown in Supplementary Fig. 10b. All the data processing steps are available in the online repository. In Supplementary Fig. 10c, d, we show that the same series resistance value also corrects an analogous measurement on the right side. In the regimes relevant to this work, the voltage divider effect caused by the series resistance does not strongly affect local conductance. On the other hand, it can be more pronounced for non-local conductance, as discussed in Supplementary Fig. 10e, f. Using the extracted resistance value, we apply the correction method described in ref. 64 to the data presented in Figs. 2–4 and Supplementary Figs. 2, 5d, 7, 8, 9d–k, and 10b, d, f, where the full conductance matrix is measured.

Device tune-up

The device is controlled with seven bottom gates (Fig. 1a). To perform tunnel spectroscopy of the hybrid segment in Supplementary Figs. 2 and 5, we use V_{LT} and V_{RT} to form a tunnel barrier and apply a large positive voltage to V_{LP}, V_{RP}, and the outer gates. V_H is used to control the electrochemical potential in the hybrid segment, where discrete states are confined because of the tunnel barriers. QDs are formed by reducing the voltage on the outer gates. This creates additional tunnel barriers next to the normal leads, thus shaping a confining potential. V_{LP} and V_{RP} control the electrochemical potential of the QDs. Finally, the coupling between the QDs and the ABS can be controlled using V_{LT} and V_{RT}. By increasing their voltage, we can achieve the strong coupling regime between the QDs and the ABS in the hybrid as explained in Fig. 1. For all the measurements presented in the main text, the gates defining the tunnel barriers were maintained at the same value.

Data availability

The raw data presented in this work, together with the code used to process and plot it, is available at https://zenodo.org/records/10013728.

Code availability

The code used for theory calculations is available at https://zenodo.org/records/10013728.

References

1. Kitaev, A. Y. Unpaired Majorana fermions in quantum wires. *Phys.-Uspekhi* **44**, 131 (2001).
2. Sau, J. D. & Sarma, S. D. Realizing a robust practical Majorana chain in a quantum-dot-superconductor linear array. *Nat. Commun.* **3**, 964 (2012).
3. Leijnse, M. & Flensberg, K. Parity qubits and poor man's Majorana bound states in double quantum dots. *Phys. Rev. B* **86**, 134528 (2012).
4. Liu, C.-X., Pan, H., Setiawan, F., Wimmer, M. & Sau, J. D. Fusion protocol for Majorana modes in coupled quantum dots. *Phys. Rev. B* **108**, 085437 (2023).
5. Boross, P. & Páyi, A. Braiding-based quantum control of a Majorana qubit built from quantum dots. *Phys. Rev. B* **109**, 125410 (2024).
6. Tsintzis, A., Souto, R. S., Flensberg, K., Danon, J. & Leijnse, M. Majorana qubits and non-abelian physics in quantum dot–based minimal Kitaev chains. *PRX Quantum* **5**, 010323 (2024).
7. Pino, D. M., Souto, R. S. & Aguado, R. Minimal Kitaev-transmon qubit based on double quantum dots. *Phys. Rev. B* **109**, 075101 (2024).
8. Liu, C.-X., Wang, G., Dvir, T. & Wimmer, M. Tunable superconducting coupling of quantum dots via Andreev bound states in semiconductor-superconductor nanowires. *Phys. Rev. Lett.* **129**, 267701 (2022).
9. Bordin, A. et al. Tunable crossed Andreev reflection and elastic cotunneling in hybrid nanowires. *Phys. Rev. X* **13**, 031031 (2023).
10. Dvir, T. et al. Realization of a minimal Kitaev chain in coupled quantum dots. *Nature* **614**, 445–450 (2023).
11. Yu, L. Bound state in superconductors with paramagnetic impurities. *Acta Phys. Sin.* **21**, 75–91 (1965).
12. Shiba, H. Classical spins in superconductors. *Prog. Theor. Phys.* **40**, 435–451 (1968).
13. Rusinov, A. Superconductivity near a paramagnetic impurity. *JETP Lett.* **9**, 85–87 (1969).

14. Buitelaar, M. R., Nussbaumer, T. & Schönenberger, C. Quantum dot in the Kondo regime coupled to superconductors. *Phys. Rev. Lett.* **89**, 256801 (2002).
15. Bauer, J., Oguri, A. & Hewson, A. C. Spectral properties of locay correlated electrons in a Bardeen-Cooper-Schrieffer superconductor. *J. Phys.: Condens. Matter* **19**, 486211 (2007).
16. Meng, T., Florens, S. & Simon, P. Self-consistent description of Andreev bound states in Josephson quantum dot devices. *Phys. Rev. B* **79**, 224521 (2009).
17. Grove-Rasmussen, K. et al. Superconductivity-enhanced bias spectroscopy in carbon nanotube quantum dots. *Phys. Rev. B* **79**, 134518 (2009).
18. Chang, W., Manucharyan, V. E., Jespersen, T. S., Nygård, J. & Marcus, C. M. Tunneling spectroscopy of quasiparticle bound states in a spinful Josephson junction. *Phys. Rev. Lett.* **110**, 217005 (2013).
19. Jeinggaard, A., Grove-Rasmussen, K., Madsen, M. H. & Nygård, J. Tuning Yu-Shiba-Rusinov states in a quantum dot. *Phys. Rev. B* **94**, 064520 (2016).
20. Grove-Rasmussen, K. et al. Yu-Shiba-Rusinov screening of spins in double quantum dots. *Nat. Commun.* **9**, 2376 (2018).
21. Tsintzis, A., Souto, R. S. & Leijnse, M. Creating and detecting poor man's Majorana bound states in interacting quantum dots. *Phys. Rev. B* **106**, 201404 (2022).
22. Fulga, I. C., Haim, A., Akhmerov, A. R. & Oreg, Y. Adaptive tuning of Majorana fermions in a quantum dot chain. *N. J. Phys.* **15**, 045020 (2013).
23. Nadj-Perge, S., Drozdov, I. K., Bernevig, B. A. & Yazdani, A. Proposal for realizing Majorana fermions in chains of magnetic atoms on a superconductor. *Phys. Rev. B* **88**, 020407 (2013).
24. Pientka, F., Peng, Y., Glazman, L. & von Oppen, F. Topological superconducting phase and Majorana bound states in Shiba chains. *Phys. Scr.* **2015**, 014008 (2015).
25. Schecter, M., Flensberg, K., Christensen, M. H., Andersen, B. M. & Paaske, J. Self-organized topological superconductivity in a Yu-Shiba-Rusinov chain. *Phys. Rev. B* **93**, 140503 (2016).
26. Nadj-Perge, S. et al. Observation of Majorana fermions in ferromagnetic atomic chains on a superconductor. *Science* **346**, 602–607 (2014).
27. Ruby, M. et al. End states and subgap structure in proximity-coupled chains of magnetic adatoms. *Phys. Rev. Lett.* **115**, 197204 (2015).
28. Jeon, S. et al. Distinguishing a Majorana zero mode using spin-resolved measurements. *Science* **358**, 772–776 (2017).
29. Schneider, L. et al. Topological Shiba bands in artificial spin chains on superconductors. *Nat. Phys.* **17**, 943–948 (2021).
30. Schneider, L. et al. Precursors of Majorana modes and their length-dependent energy osciations probed at both ends of atomic Shiba chains. *Nat. Nanotechnol.* **17**, 384–389 (2022).
31. Liu, C.-X. et al. Enhancing the excitation gap of a quantum-dot-based Kitaev chain. *Commun. Phys.* **7**, 1–7 (2024).
32. ten Haaf, S. L. D. et al. A two-site Kitaev chain in a two-dimensional electron gas. *Nature* **630**, 329–334 (2024).
33. Badawy, G. et al. High mobility stemless InSb nanowires. *Nano Lett.* **19**, 3575–3582 (2019).
34. Hornibrook, J. M. et al. Frequency multiplexing for readout of spin qubits. *Appl. Phys. Lett.* **104**, 103108 (2014).
35. Wang, J.-Y. et al. Parametric exploration of zero-energy modes in three-terminal InSb-Al nanowire devices. *Phys. Rev. B* **106**, 075306 (2022).
36. Heedt, S. et al. Shadow-wa lithography of baistic superconductor-semiconductor quantum devices. *Nat. Commun.* **12**, 4914 (2021).
37. Borsoi, F. et al. Single-shot fabrication of semiconducting-superconducting nanowire devices. *Adv. Funct. Mater.* **31**, 2102388 (2021).
38. Mazur, G. P. et al. Spin-mixing enhanced proximity effect in aluminum-based superconductor-semiconductor hybrids. *Adv. Mater.* **34**, 2202034 (2022).
39. Reeg, C., Loss, D. & Klinovaja, J. Metaization of a Rashba wire by a superconducting layer in the strong-proximity regime. *Phys. Rev. B* **97**, 165425 (2018).
40. Kiršanskas, G., Goldstein, M., Flensberg, K., Glazman, L. I. & Paaske, J. Yu-Shiba-Rusinov states in phase-biased superconductor–quantum dot–superconductor junctions. *Phys. Rev. B* **92**, 235422 (2015).
41. Piet, J.-D. et al. Andreev bound states in supercurrent-carrying carbon nanotubes revealed. *Nat. Phys.* **6**, 965–969 (2010).
42. Lee, E. J. H. et al. Spin-resolved Andreev levels and parity crossings in hybrid superconductor-semiconductor nanostructures. *Nat. Nanotechnol.* **9**, 79–84 (2014).
43. Scherübl, Z. et al. Large spatial extension of the zero-energy Yu-Shiba-Rusinov state in a magnetic field. *Nat. Commun.* https://doi.org/10.1038/s41467-020-15322-9 (2020).
44. Scherübl, Z. et al. From cooper pair splitting to nonlocal spectroscopy of a Shiba state. *Phys. Rev. Res.* https://doi.org/10.1103/PhysRevResearch.4.023143 (2022).
45. Schindele, J., Baumgartner, A., Maurand, R., Weiss, M. & Schönenberger, C. Nonlocal spectroscopy of Andreev bound states. *Phys. Rev. B* **89**, 045422 (2014).
46. Gramich, J., Baumgartner, A. & Schönenberger, C. Andreev bound states probed in three-terminal quantum dots. *Phys. Rev. B* **96**, 1–14 (2017).
47. Wang, G. et al. Singlet and triplet Cooper pair splitting in hybrid superconducting nanowires. *Nature* **612**, 448–453 (2022).
48. Trocha, P. & Weymann, I. Spin-resolved Andreev transport through double-quantum-dot cooper pair splitters. *Phys. Rev. B* https://doi.org/10.1103/PhysRevB.91.235424 (2015).
49. Scherübl, Z., Pályi, A. & Csonka, S. Transport signatures of an Andreev molecule in a quantum dot–superconductor–quantum dot setup. *Beilstein J. Nanotechnol.* **10**, 363–378 (2019).
50. Saldaña, J.C.E. et al. Two-impurity Yu-Shiba-Rusinov states in coupled quantum dots. *Phys. Rev. B* https://doi.org/10.1103/PhysRevB.102.195143 (2020).
51. Kürtössy, O. et al. Andreev molecule in parael InAs nanowires. *Nano Lett.* **21**, 7929–7937 (2021).
52. Aasen, D. et al. Milestones toward Majorana-based quantum computing. *Phys. Rev. X* **6**, 031016 (2016).
53. Knapp, C., Karzig, T., Lutchyn, R. M. & Nayak, C. Dephasing of Majorana-based qubits. *Phys. Rev. B* **97**, 125404 (2018).
54. Mishmash, R. V., Bauer, B., von Oppen, F. & Alicea, J. Dephasing and leakage dynamics of noisy Majorana-based qubits: Topological versus Andreev. *Phys. Rev. B* **101**, 075404 (2020).
55. Boross, P. & Pályi, A. Dephasing of Majorana qubits due to quasistatic disorder. *Phys. Rev. B* **105**, 035413 (2022).
56. Bordin, A. et al. Signatures of Majorana protection in a three-site Kitaev chain. *arXiv* https://doi.org/10.48550/arXiv.2402.19382 (2024).
57. Hays, M. et al. Coherent manipulation of an Andreev spin qubit. *Science* **373**, 430–433 (2021).
58. Pita-Vidal, M. et al. Direct manipulation of a superconducting spin qubit strongly coupled to a transmon qubit. *Nat. Phys.* **19**, 1110–1115 (2023).
59. Choi, M.-S., Bruder, C. & Loss, D. Spin-dependent Josephson current through double quantum dots and measurement of entangled electron states. *Phys. Rev. B* **62**, 13569–13572 (2000).
60. Leijnse, M. & Flensberg, K. Coupling spin qubits via superconductors. *Phys. Rev. Lett.* **111**, 060501 (2013).
61. Hensgens, T. et al. Quantum simulation of a Fermi-Hubbard model using a semiconductor quantum dot array. *Nature* **548**, 70–73 (2017).

62. Dehoain, J. P. et al. Nagaoka ferromagnetism observed in a quantum dot plaquette. *Nature* **579**, 528–533 (2020).
63. Hsiao, T.-K. et al. Exciton transport in a germanium quantum dot ladder. *Phys. Rev. X* **14**, 011048 (2024).
64. Martinez, E. A. et al. Measurement circuit effects in three-terminal electrical transport measurements. *arXiv* https://doi.org/10.48550/arXiv.2104.02671 (2021).

Acknowledgements

This work has been supported by the Dutch Organization for Scientific Research (NWO) and Microsoft Corporation Station Q. We thank John M. Hornibrook and David J. Reilly for providing the frequency multiplexing chips. We thank Martin Leijnse, Ville Maisi, Pasquale Scarlino, Athanasios Tsintzis, Rubén Seoane Souto, Karsten Flensberg, Srijit Goswami, Sebastiaan L. D. ten Haaf, Qingzhen Wang, Ivan Kulesh, and Yining Zhang for helpful discussions.

Author contributions

D.v.D., F.Z., A.B., G.P.M., N.v.L., and J.C.W. fabricated the device. F.Z., D.v.D., D.X., B.R., and T.D. performed the electrical measurements. T.D. and G.W. designed the experiment. F.Z., D.v.D., G.W., and T.D. analyzed the data. F.Z., D.v.D., T.D., G.W., and L.P.K. prepared the manuscript with input from all authors. T.D. and L.P.K. supervised the project. C.X.L. and A.M.B. developed the theoretical model with input from M.W.; G.B., S.G., and E.P.A.M.B. performed InSb nanowire growth.

Competing interests

The authors declare no competing interests.

Additional information

Supplementary information The online version contains supplementary material available at https://doi.org/10.1038/s41467-024-52066-2.

Correspondence and requests for materials should be addressed to Leo P. Kouwenhoven.

Peer review information *Nature Communications* thanks the anonymous reviewers for their contribution to the peer review of this work. A peer review file is available.